

Highly-dispersed ultrafine Pt nanoparticles on reduced graphene oxide nanosheets: In situ sacrificial template synthesis and superior electrocatalytic performance for methanol oxidation

Shouliang Wu ^a, Jun Liu ^a, Zhenfei Tian ^a, Yunyu Cai ^a, Yixing Ye ^a, Qinglin Yuan ^{a, b} and Changhao Liang ^{a, b*}

^aKey Laboratory of Materials Physics and Anhui Key Laboratory of Nanomaterials and Nanotechnology, Institute of Solid State Physics, Chinese Academy of Sciences, Hefei 230031, China.

^bDepartment of Materials Science and Engineering, University of Science and Technology of China, Hefei 230026, China.

*Corresponding author. Tel: +86 55165591129; Fax: Tel: +86 55165591434;
E-mail: chliang@issp.ac.cn

Keywords: ultrafine Pt NPs, electrocatalyst, *in situ* sacrificial template, laser ablation in liquids, methanol oxidation.

Abstract

We report a simple and environment-friendly route to prepare platinum/reduced graphene oxide (Pt/rGO) nanocomposites (NCs) with highly reactive MnO_x colloids as reducing agents and sacrificial templates. The colloids are obtained by laser ablation of a metallic Mn target in graphene oxide (GO)-containing solution. Structural and morphological investigations of the as-prepared NCs revealed that ultrafine Pt nanoparticles (NPs) with an average size of 1.8 (\pm 0.6) nm are uniformly dispersed on the surfaces of rGO nanosheets. Compared with commercial Pt/C catalysts, Pt/rGO NCs with highly electrochemically active surface areas show remarkably improved catalytic activity and durability toward methanol oxidation. All of these superior characteristics can be attributed to the small particle size and uniform distribution of the Pt NPs, as well as the excellent electrical conductivity and stability of the rGO catalyst support. These findings suggest that Pt/rGO electrocatalysts are promising candidate materials for practical use in fuel cells.

Introduction

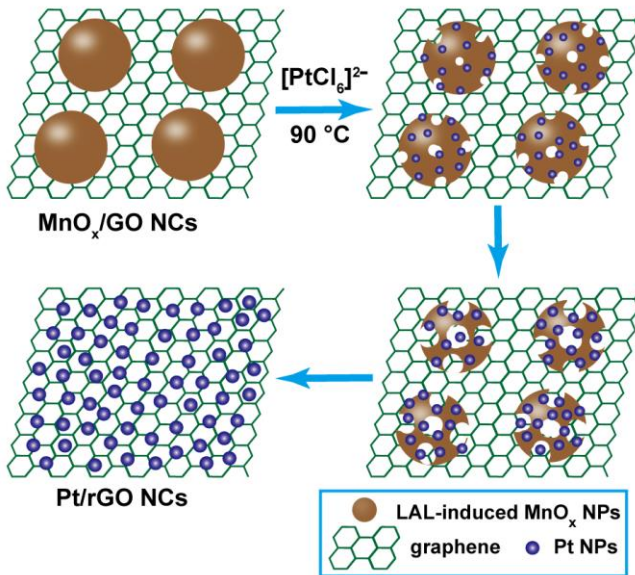
Among the different clean and renewable energy systems currently available, direct methanol fuel cells (DMFCs) have been extensively studied in recent decades because of their simple structure, high power densities, high energy conversion efficiencies, low operation temperatures, and low pollutant emissions.^{1–5} In these electrochemical cells, methanol is directly oxidized by oxygen from air into water and carbon dioxide to generate electricity. Pt-based materials are widely used as anode electrocatalysts for driving methanol oxidation reactions. However, the high manufacturing cost and slow reaction kinetics of Pt-based catalysts have seriously prevented the successful commercialization of DMFCs. Considering these issues, great effort has been made to develop non-Pt-containing catalysts. Thus far, only a few catalysts have shown sufficiently acceptable electrocatalytic activity.^{6, 7} Therefore, Pt-based catalysts with reduced costs and improved catalytic activities must be developed.

The size of Pt NPs is known to be one of the most important factors affecting the performance of a catalyst. As the particle size decreases, a large fraction of active Pt atoms could be exposed to the surfaces; thus, ultrafine Pt NPs often exhibit highly enhanced catalytic activities. Downsizing Pt NPs is another way to reduce the Pt loading and cost of catalysts. However, when the size of the Pt NPs is too small, the high surface energy of the NPs may cause severe aggregation, thereby inducing a serious decline in their performance during catalytic operation and impeding their use in industrial processes.^{8, 9} An effective strategy for solving these deactivation problems involves uniform loading of the Pt NP catalysts onto a carrier with a large surface area and good electrical conductivity.

Vulcan XC-72 carbon is commonly used as the support material for dispersed nano-sized Pt catalysts.¹⁰ However, this material is susceptible to corrosion at the operating conditions of

DMFCs, such as in systems with acidic electrolytes ($\text{pH} < 1$) and high driving potentials (0.6–1.2 V).^{11, 12} Thus, semiconductive oxides and carbides, such as TiO_2 ¹³, CeO_2 ¹⁴, SiC ¹⁵ and B_4C ¹⁶, have been investigated as catalyst support materials because of their high electrochemical activity and stability. However, their low electrical conductivity seriously impedes their further development as suitable catalyst supports for DMFCs. Graphene is a monolayer of carbon atoms packed into a dense honeycomb crystal structure; this material has recently attracted increased attention because of its potential application as a catalyst support in fuel cells.^{17–20} Pt NPs can be deposited on graphene sheets to achieve specific properties, such as a large surface area to provide high metal dispersion, a high electrical conductivity to facilitate electron transfer, a suitable porosity to promote gas flow, and a high stability to avoid corrosion in both acidic and alkaline media.

In this study, we propose a simple and green strategy to fabricate Pt/rGO NCs based on laser ablation in liquids (LAL). LAL-generated MnO_x colloids with high reactivity can be used as agents to reduce GO and PtCl_6^{2-} , and MnO_x NPs can be easily deposited onto graphene nanosheets and further used as *in situ* sacrificial templates to ensure the uniform distribution of reduced Pt NPs on the surface of rGO nanosheets. A schematic of the proposed transformation is shown in **Scheme 1**. To identify their potential utility in catalytic applications, the electrocatalytic activity of the as-prepared Pt/rGO NCs was tested for methanol oxidation. The NC catalysts obtained displayed remarkably enhanced electrocatalytic performance toward methanol oxidation as compared with commercial Pt/C catalysts.



Scheme 1. Schematic illustration for the formation of Pt/rGO NCs.

Experimental section

Chemical reagents and materials

All chemicals used in this experiment were of analytical grade and applied without further purification. Graphite powder was purchased from Tianjin Guangfu Fine Chemical Research Institute. GO (TEM image in Figure S1) was fabricated according to a modified Hummers method.^{21, 22} The commercial Pt/C catalysts (20 wt% Pt on Vulcan XC72R carbon) were purchased from Johnson Matthey. Double-distilled water (resistance, $>18 \text{ M}\Omega \text{ cm}^{-1}$) was used throughout all experiments.

Preparation of Pt/rGO NCs

After fixing a manganese metal plate (99.8% purity) to a vessel filled with 15 mL GO solution, the rotating metal plate was ablated for 15 min by a fundamental Nd:YAG laser (1064 nm) with a 10 Hz pulse repetition rate, 10 ns pulse duration, and 100 mJ per pulse laser energy. After

ablation, the fresh colloids and 2 mL chloroplatinic acid ($\text{H}_2\text{PtCl}_6 \cdot 6\text{H}_2\text{O}$, 4 mg mL^{-1}) were fed into a round flask (100 mL) in an oil bath heated to 90 °C for 24 h. During oil bath heating, the solution was intensely stirred. To investigate the formation of the Pt/rGO NCs, 1 mL of the suspension was sampled at different reaction intervals (8 and 18 h). The black precipitate was collected by centrifugation and alternately washed with deionized water and anhydrous ethanol for three times. The final products were obtained by drying the precipitate at 60 °C in a vacuum-drying box.

Characterization

The phase structures of the prepared products were analyzed by a Rigaku X-ray diffractometer with Cu $\text{K}\alpha$ radiation ($\lambda = 0.15419$ nm). Raman spectra were measured by a confocal Raman microprobe (RENISHAW in Via Raman Microscope) with 532 nm argon ion laser excitation. The surface chemical constituents of the products were analyzed by X-ray photoelectron spectroscopy (XPS, Thermo ESCACLB 250). Fourier transform infrared (FT-IR) spectra were recorded on a Nicolet 8700 spectrometer by the KBr pellet technique. High-resolution transmission electron microscopy (HR-TEM) was performed on a JEOL-2010 apparatus with 200 kV accelerating voltage. The TEM specimen was made by dispersing the product powders in ethanol to form a suspension, which was then dropped onto a carbon-coated Cu grid after ultrasonic treatment. Electrochemical impedance spectroscopy (EIS) of the products was performed with a Zahner IM6e electrochemical workstation.

Electrochemical measurements

All electrochemical measurements were conducted at room temperature in a standard three-electrode Zahner IM6e electrochemical workstation. A KCl-saturated Ag/AgCl electrode and a Pt wire were used as the reference and counter electrodes, respectively. A glassy carbon (GC)

electrode (3 mm in diameter) was polished to a mirror finish with Al₂O₃ slurry (0.3 µm) and ultrasonically cleaned in ethanol for a few minutes. Subsequently, 10 µL of the as-obtained Pt/rGO NCs or commercial Pt/C catalyst suspension was directly pipetted onto a working electrode, followed by solvent evaporation at room temperature. Exactly 20 µL of the Nafion solutions were then dropped onto each dried sample. The weight concentration of Pt in the catalyst suspension was estimated through inductively coupled plasma optical emission spectrometry (ICP-OES). Cyclic voltammetry (CV) experiments were performed in a 0.5 M N₂-saturated H₂SO₄ aqueous solution at a scan rate of 50 mV s⁻¹. The electrocatalytic activity for methanol oxidation of the catalysts was measured in a mixture of 0.5 M methanol and 0.5 M H₂SO₄ (or 0.5 M KOH). The current–time (CA) curves of the catalysts were recorded at 0.635 V or -0.192 V for 3600 s. Long-term CV tests (1000 cycles) were conducted in acidic and alkaline media at a scan rate of 50 mV s⁻¹ to assess the stability of the Pt/rGO catalysts further.

Results and discussion

The morphology of the as-synthesized Pt/rGO NCs was characterized by TEM. As seen from the low-magnification TEM images (Figures 1a–1c), large quantities of Pt NPs are highly dispersed on the surface of rGO nanosheets, which shows a very narrow size distribution with average size of 1.8 (± 0.6) nm (inset of Figure 1c). The HR-TEM image of the Pt/rGO NCs in Figure 1d reveals the ordered lattice fringes of Pt NPs. The *d*-spacing value of 0.226 nm coincides well with that of face-centered cubic Pt (111), which is also consistent with the XRD peaks in Figure 2a. Moreover, even after a long period of drastic sonication, the Pt NPs were still firmly and uniformly anchored on the surface of rGO sheets, thereby indicating strong interactions between the Pt NPs and rGO sheets. Therefore, the rGO nanosheets play an important role in preventing agglomeration of ultrafine Pt NPs. Conversely, the highly dispersed

Pt NPs on the surface of rGO sheets can act as “spacers” to prevent the overlapping of rGO sheets.

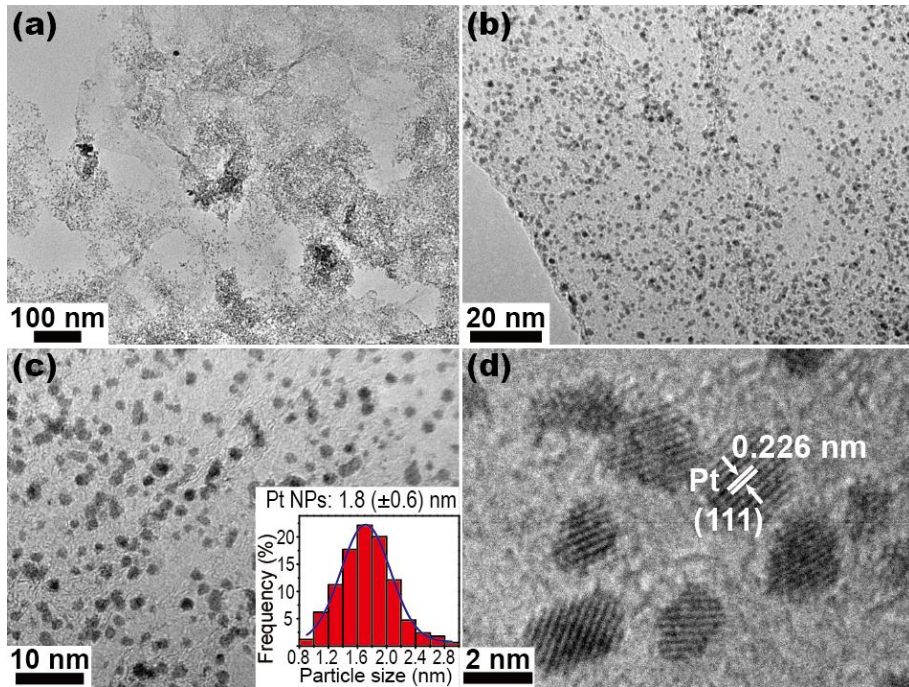


Figure 1. Low-magnification TEM (a–c) and HR-TEM (d) images of the as-prepared Pt/rGO NCs. The inset in (c) shows the particle size-distribution histogram of Pt NPs.

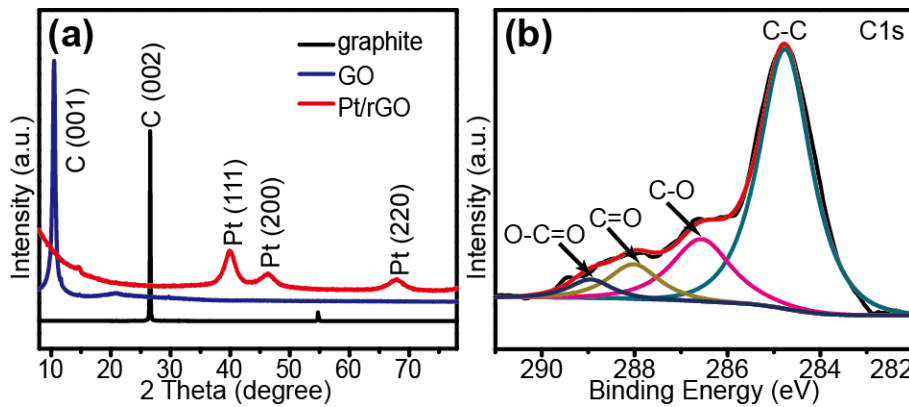


Figure 2. (a) XRD patterns of pristine graphite, GO, and Pt/rGO NCs. (b) High-resolution C 1s XPS spectra of Pt/rGO NCs.

The XRD patterns of pristine graphite (black line), graphene oxide (GO, blue line), and as-prepared Pt/rGO NCs (red line) are shown in Figure 2a. The XRD peak of pristine graphite is observed at a 2θ value of 26.6° , which indicates an interlayer distance of 0.335 nm. This peak shifts to 10.5° after oxidation treatment, which suggests that the interlayer distance in GO increases to 0.82 nm.^{23, 24} The interlayer distance in GO expands because of the presence of epoxide, hydroxyl, and carboxyl groups, as well as water molecules, between the GO layers, which cause the GO to become hydrophilic. These surface functional groups can act as anchoring sites for metallic compounds. As soon as the Pt/rGO NCs are formed, no obvious peaks attributable to pristine graphite or GO could be observed. Many previous studies have shown that, if the regular stacks of graphite or GO are destroyed, for example, by exfoliation, their diffraction peaks would become weaker or even disappear.²³ Therefore, combined with the above morphological analysis, it can be concluded that the graphene nanosheets could be destroyed by the decorated Pt NPs.²⁴ Diffraction peaks at 2θ values of 40.0° , 46.5° , and 67.9° correspond to the (111), (200), and (220) facets, respectively, of face-centered cubic Pt crystals (JCPDS No. 01-1194), which confirms that the Pt precursor has been chemically reduced to Pt NPs. Peaks corresponding to manganese-based oxides were not observed, which demonstrates that the initial MnO_x NPs have completely reacted.

Figure 2b displays the high-resolution C 1s XPS spectra of Pt/rGO NCs, which can be divided into four peaks corresponding to carbon atoms in different oxygen-containing functional groups. The peak located at a binding energy of 284.8 eV is assigned to the C–C bond. Three other peaks located at binding energies of 286.4, 287.9, and 288.9 eV respectively correspond to the C–O, C=O, and O–C=O bonds, which show much weaker intensity compared with the peak of the C–C bond. By comparing the high-resolution C 1s XPS spectrum from GO (Figure S5), the peak

intensity of oxygen-containing functional groups sharply decreased, indicating that GO was reduced into rGO.^{23, 25} Consistent with our Raman (Figure S2) and FT-IR (Figure S3) analyses, the results described above reveal that reduction of GO and loading of ultrafine Pt NPs onto rGO nanosheets were successfully achieved via a one-pot treatment.

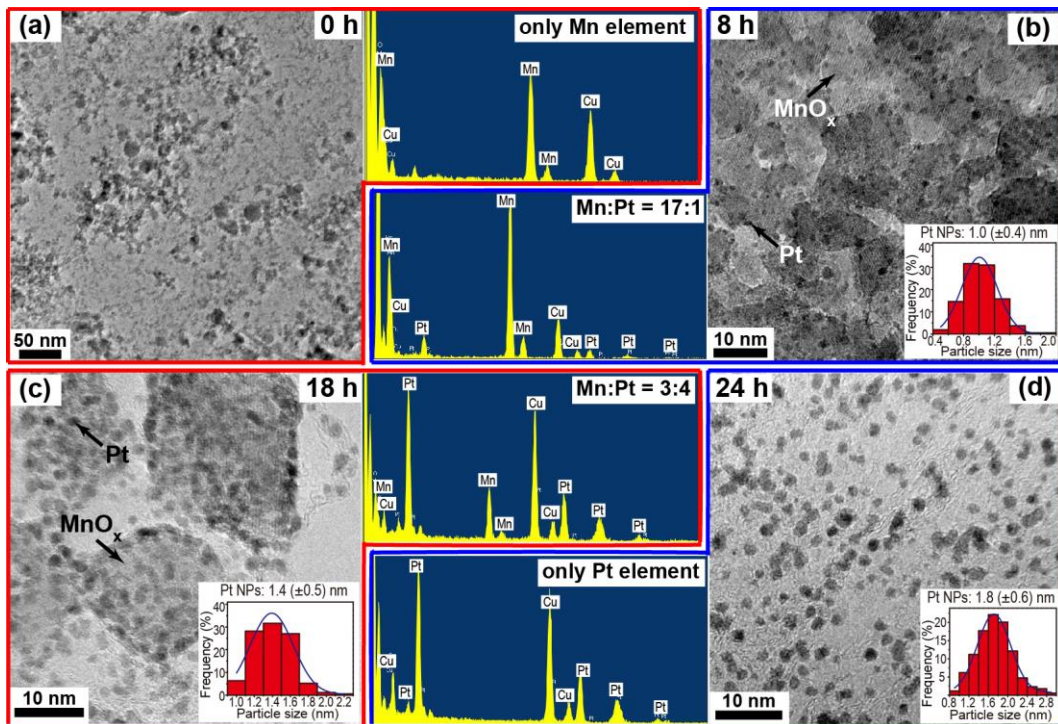


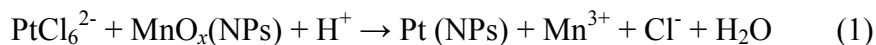
Figure 3. TEM images and corresponding EDS spectra obtained from the reaction suspension at different reaction intervals: (a) 0 h, (b) 8 h, (c) 18 h, and (d) 24 h. The insets illustrate the particle size-distribution histograms of Pt NPs. The peaks assigned to Cu elements during EDS analysis are attributed to the Cu grid used for TEM measurement.

We propose the formation mechanism of Pt/rGO NCs in our synthesis strategy as follows. In our previous work, we confirmed that fresh colloids generated by the LAL technique possess high activity and reactivity.^{26–28} For example, LAL-induced SnO_x colloids can be used as reducing agents and composite precursors to prepare SnO₂/rGO NCs.²⁹ In the present experiment,

when the laser beam hits the surface of the Mn target, a Mn cluster containing a plasma plume with high temperature and high pressure is instantaneously produced at the solid-liquid interface. Subsequent ultrasonic and adiabatic expansion of the plume region forms small MnO_x clusters with a low valence state. These MnO_x clusters retain their relatively high-temperature and high-pressure state; thus, the clusters are expected to be very active and quickly oxidized with the simultaneous reduction of GO to some extent. Highly active MnO_x NPs can also be well dispersed on the GO sheets to form MnO_x/GO NCs (Figure 3a). These NCs are mainly composed of Mn_3O_4 and MnO NPs, which are described as MnO_x (XRD pattern is shown in Figure S4). Partial reduction of GO can be confirmed by the high-resolution C 1s XPS spectra of GO and MnO_x/GO NCs (Figure S5). The peak intensities of the oxygen-containing functional groups of MnO_x/GO NCs sharply decreased compared with those of GO, which indicates the reduction of GO to some extent. As soon as the Pt/rGO NCs are formed, the peak intensity of oxygen with its functionalities is further decreased, thereby revealing further reduction of GO during the oil bath heating process. These findings may be further confirmed by the FT-IR analysis results (Figure S3).

To understand the formation process of the Pt NPs better, we obtained TEM images and the corresponding EDS spectra from the products obtained from the reaction suspension at different reaction intervals (Figure 3). When the MnO_x/GO NCs were immersed in an aqueous solution of H_2PtCl_6 at 90 °C, Pt nanocrystals were spontaneously formed on the surface of the MnO_x NPs, where multiple numbers of tiny Pt nanocrystals, with an average size of 1.0 (± 0.4) nm, were attached to the surface of MnO_x NPs, as shown in Figure 3b. However, the longer reaction duration (Figure 3c) could cause additional nucleation and extensive deposition of Pt nanocrystals with slightly larger particle sizes. The TEM and EDS analysis results reveal that the

MnO_x NPs progressively dissolve during the reaction, which implies that the growth of Pt proceeds via step-by-step consumption of MnO_x . Therefore, the TEM images of products with a reaction time of 24 h show the generation of Pt/rGO NCs, wherein the 1.8 (± 0.6) nm-sized Pt NPs are densely and uniformly dispersed on the rGO sheets (Figure 3d). The corresponding EDS spectra of the Pt/rGO NCs show peaks corresponding to C and Pt elements, which further confirms the formation of Pt NPs. This reaction can be described by the following equation:



To evaluate the potential application of as-prepared Pt/rGO NCs, we investigated their electrochemical properties for methanol oxidation in both acidic and alkaline media. For comparison, the electrochemical measurements were also carried out with commercial Pt/C catalysts under the same conditions. The morphology and component characterization of the commercial Pt/C catalysts are presented in Figure S6.

The electrochemical surface area (ECSA) of Pt catalysts is an important factor determining its catalytic activity. Figure 4a shows the typical CVs of prepared Pt/rGO and commercial Pt/C catalysts measured in a 0.5 M N_2 -saturated H_2SO_4 aqueous solution. Typical hydrogen adsorption and desorption were observed between -0.2 V and 0.16 V (vs. Ag/AgCl). The CV curve of Pt/rGO catalysts shows peaks with a current density in the hydrogen adsorption/desorption region higher than those of the commercial Pt/C catalysts. The ECSA of the catalysts can be calculated on the basis of the hydrogen adsorption region according to the following equation:^{11, 30}

$$\text{ECSA} = Q_{\text{H}} / (0.21 \times [\text{Pt}]) \quad (2)$$

where 0.21 (in mC cm^{-2}) is assumed as the monolayer charge (calculated from the surface density of 1.3×10^{15} atom cm^{-2}), Q_{H} (in mC cm^{-2}) is the amount of charge exchanged during the

electro-desorption of hydrogen atoms on Pt, and [Pt] (in mg cm^{-2}) is the loading amount of Pt on the working electrode. The calculated ECSA of the prepared Pt/rGO catalysts is $1013.4 \text{ cm}^2 \text{ mg}^{-1}$, which is larger than that of the commercial Pt/C catalysts ($826.9 \text{ cm}^2 \text{ mg}^{-1}$). The large ECSA value of the Pt/rGO catalysts indicates the ultrafine size and uniform dispersion of Pt NPs on the rGO nanosheets, which is in good agreement with the observed morphology.

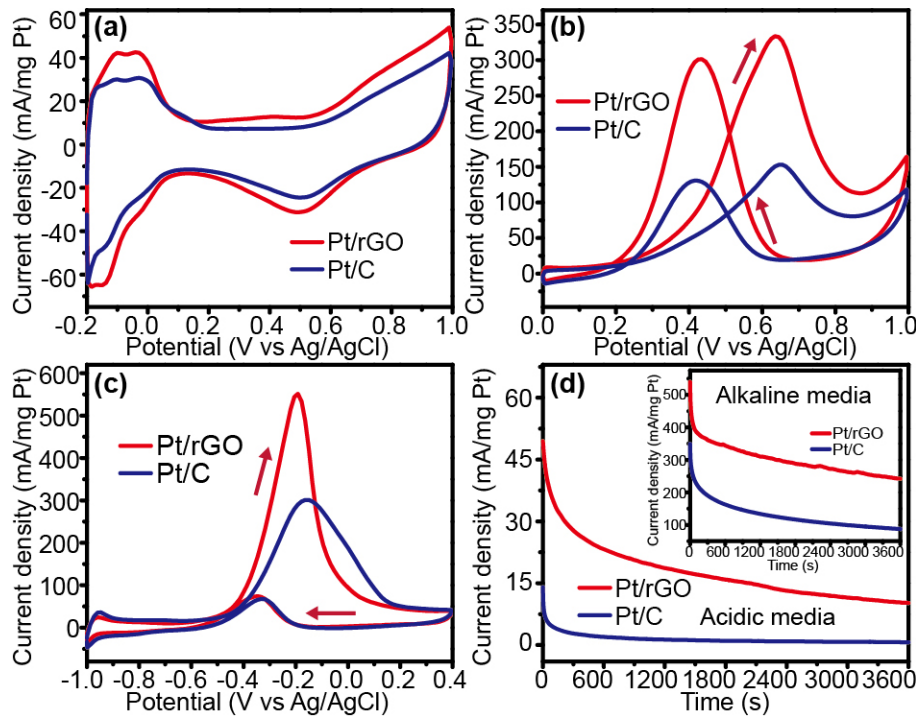


Figure 4. CV curves of GC electrodes modified with prepared Pt/rGO and commercial Pt/C catalysts measured at a scan rate of 50 mV s^{-1} in $0.5 \text{ M N}_2\text{-saturated H}_2\text{SO}_4$ (a), $0.5 \text{ M H}_2\text{SO}_4 + 0.5 \text{ M CH}_3\text{OH}$ (b), and $0.5 \text{ M KOH} + 0.5 \text{ M CH}_3\text{OH}$ (c). CA curves of prepared Pt/rGO and commercial Pt/C catalysts measured in $0.5 \text{ M H}_2\text{SO}_4 + 0.5 \text{ M CH}_3\text{OH}$ (d) and $0.5 \text{ M KOH} + 0.5 \text{ M CH}_3\text{OH}$ (inset) at a scan rate of 50 mV s^{-1} .

The mass activity of the Pt-based catalysts, which is defined as the peak current per amount of Pt loading, is commonly adopted for evaluating their electrocatalytic performances. Figure 4b shows typical CVs obtained in a $0.5 \text{ M H}_2\text{SO}_4$ solution containing $0.5 \text{ M CH}_3\text{OH}$. The prepared

Pt/rGO catalysts show obviously higher current density at all corresponding potentials compared with the commercial Pt/C catalysts. Figure 4b demonstrates that the forward peak current density of the Pt/rGO catalysts is 333.3 mA mg^{-1} or about 2.17 times that of the commercial Pt/C catalysts (153.3 mA mg^{-1}). Similarly, in acidic media, the Pt/rGO catalysts exhibited a higher forward peak current density (552.5 mA mg^{-1}) than the commercial Pt/C catalysts (301.7 mA mg^{-1}) in alkaline media, as shown in Figure 4c. More importantly, the Pt/rGO catalysts exhibited better CO tolerance in alkaline media. Previous reports have confirmed that the ratio of peak current densities for the forward (I_f) and backward (I_b) scans is an indicator of the CO tolerance of the catalyst.^{31,32} A higher I_f/I_b value indicates higher tolerance to intermediate carbon species, which means methanol can be oxidized into carbon dioxide much more efficiently. According to the calculation based on the Figure 4c, the I_f/I_b value for the Pt/rGO catalysts is 7.45, which is much higher than that of the commercial Pt/C catalysts (4.46). To describe the electrocatalytic performance of the prepared Pt/rGO catalysts further, the specific activities observed were also compared with those of commercial Pt/C catalysts, as shown in Figure S7. Results reveal that the specific activities of Pt/rGO catalysts are much higher than those of the commercial Pt/C catalysts in acidic and alkaline media. All of these results provide clear evidence of the superior electrocatalytic activity of the prepared Pt/rGO catalysts for methanol oxidation.

The stabilities of the prepared Pt/rGO and commercial Pt/C catalysts were examined by steady-state chronoamperometry, as shown in Figure 4d. Compared with the commercial Pt/C catalysts, the Pt/rGO catalysts exhibited obviously higher initial current densities and maintained higher current densities during the entire test range in acidic and alkaline media; these findings indicate a higher poison-tolerance to absorbed intermediates generated during the methanol oxidation processes. To prove the stability of the Pt/rGO catalysts further, long-term CV tests

were conducted in both acidic and alkaline media. As shown in Figures 5a and 5d, no obvious changes were found in the shape and peak potential of the CV curves of the Pt/rGO catalysts after the CA test and the subsequent 1000 cycles. In acidic media (Figures 5a–5c), the remaining peak current density of the Pt/rGO catalysts was calculated as 93.0% relative to the initial value after the CA test, which is higher than that observed from the commercial Pt/C catalysts (75.9%). Even at the 1000th cycle, the peak current density of Pt/rGO catalysts remained at 85.6%, but the corresponding value obtained from the commercial Pt/C catalysts sharply dropped to 62.4%. The same phenomena were observed in alkaline media (Figure 5d–5f). The calculated forward peak current for the Pt/rGO catalysts was 88.6% after the CA test and 77.9% after 1000 cycles, both of which are higher than those of the commercial Pt/C catalysts (85.1% and 61.4%, respectively). These results suggest that the Pt/rGO catalysts have excellent oxidation ability and corrosion resistance.

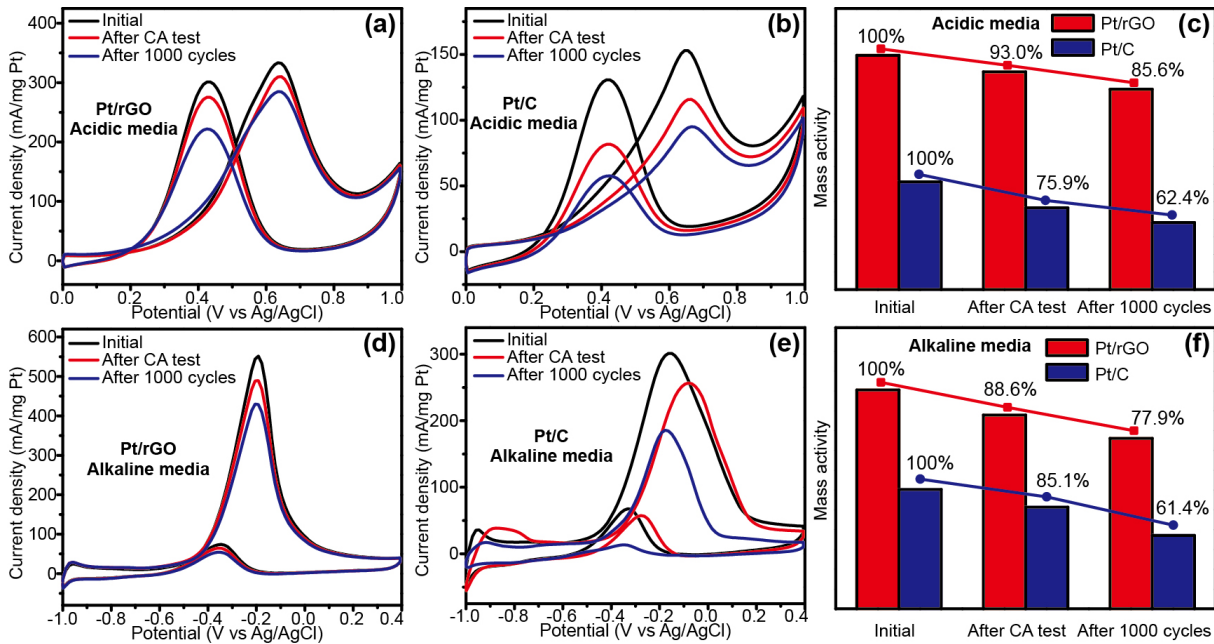


Figure 5. CV curves of prepared Pt/rGO and commercial Pt/C catalysts measured in 0.5 M H_2SO_4 + 0.5 M CH_3OH (a–c) and 0.5 M KOH + 0.5 M CH_3OH (d–f) at the initial, after CA test and the subsequent 1000 cycles.

The good performance of as-prepared Pt/rGO catalysts in methanol oxidation can be reasonably understood by considering the following facts. First, compared with other carbon support materials, graphene possesses a larger surface area that can efficiently prevent the Pt NPs from coalescing and thus lead to the formation of highly dispersed, high-density, and ultrafine Pt NPs. These well-dispersed and ultrafine Pt NPs are endowed with more electrochemically active sites, active facets, and an active surface area. As well, the excellent stability of graphene can retain the structural integrity of the Pt/rGO catalysts under harsh electrochemical conditions. More importantly, graphene has excellent conductivity and can cause rapid transport of electron or charge carriers. To investigate the nature of these electrons or charge transfers, typical EIS data are presented as Nyquist plots in Figure S8. The diameter of the semicircle in the plot of the prepared Pt/rGO catalysts is much smaller than that observed for commercial Pt/C catalysts, and this feature indicates a much smaller solid-state interfacial resistance and electron or charge transfer resistance. These multiple factors contribute to the remarkable catalytic performance of the prepared Pt/rGO catalysts.

Conclusions

In summary, high-quality Pt/rGO NCs were successfully synthesized with graphene-anchored MnO_x NPs as a reaction template. Compared with commercial Pt/C catalysts, the as-prepared Pt/rGO catalysts possess higher activity and better long-term performance for methanol electro-oxidation in acidic and alkaline media, which indicates that our electrocatalysts can provide more

efficient Pt utilization. Graphene shows great potential application as a catalyst carrier in fuel cells. The proposed synthetic method is simple, effective, and environment-friendly, and the technique may be extended to the preparation of other noble metals or their alloys NPs on graphene for electrocatalytic or electrochemical sensor applications.

Associated Content

Supporting Information

Characterization of prepared GO and commercial Pt/C catalysts, additional Raman, FT-IR, XRD and XPS analysis of the products, EIS spectra of Pt/rGO and commercial Pt/C catalysts. This material is available free of charge via the Internet at <http://pubs.acs.org>.

Author Information

Corresponding Author

Tel: +86 55165591129; Fax: Tel: +86 55165591434; E-mail: chliang@issp.ac.cn

Notes

The authors declare no competing financial interest.

Acknowledgments

This work was financial supported by the National Basic Research Program of China (2014CB931704), the National Natural Science Foundation of China (NSFC, No. 11174287, 51371166, 11204308) and CAS Key Technology Talent Program.

References

- (1) Liu, H. S.; Song, C. J.; Zhang, L.; Zhang, J. J.; Wang, H. J.; Wilkinson, D. P. A Review of Anode Catalysis in the Direct Methanol Fuel Cell. *J. Power Sources* **2006**, *155*, 95–110.
- (2) Service, R. F. Shrinking Fuel Cells Promise Power in Your Pocket. *Science* **2002**, *296*, 1222–1224.
- (3) Shen, Y.; Zhang, Z. H.; Long, R. R.; Xiao, K. J.; Xi, J. Y. Synthesis of Ultrafine Pt Nanoparticles Stabilized by Pristine Graphene Nanosheets for Electro-oxidation of Methanol. *ACS Appl. Mater. Interfaces* **2014**, *6*, 15162–15170.
- (4) Chen, A. C.; Holt-Hindle, P. Platinum-Based Nanostructured Materials: Synthesis, Properties, and Applications. *Chem. Rev.* **2010**, *110*, 3767–3804.
- (5) Huang, H. J.; Wang, X. Recent Progress on Carbon-based Support Materials for Electrocatalysts of Direct Methanol Fuel Cells. *J. Mater. Chem. A* **2014**, *2*, 6266–6291.
- (6) Serov, A.; Kwak, C. Review of Non-platinum Anode Catalysts for DMFC and PEMFC Application. *Appl. Catal., B* **2009**, *90*, 313–320.
- (7) Gu, L.; Qian, L.; Lei, Y.; Wang, Y. Y.; Li, J.; Yuan, H. Y.; Xiao, D. Microwave-assisted Synthesis of Nanosphere-like NiCo₂O₄ Consisting of Porous Nanosheets and its Application in Electro-catalytic Oxidation of Methanol. *J. Power Sources* **2014**, *261*, 317–323.
- (8) Kim, K. W.; Kim, S. M.; Choi, S. H.; Kim, J. W.; Lee, I. S. Electroless Pt Deposition on Mn₃O₄ Nanoparticles via the Galvanic Replacement Process: Electrocatalytic Nanocomposite with Enhanced Performance for Oxygen Reduction Reaction. *ACS Nano* **2012**, *6*, 5122–5129.

- (9) Tang, Y. N.; Yang, Z. X.; Dai, X. Q. A Theoretical Simulation on the Catalytic Oxidation of CO on Pt/graphene. *Phys. Chem. Chem. Phys.* **2012**, *14*, 16566–16572.
- (10) Qiu, Z.; Huang, H.; Du, J.; Feng, T.; Zhang, W. K.; Gan, Y. P.; Tao, X. Y. NbC Nanowire-Supported Pt Nanoparticles as a High Performance Catalyst for Methanol Electrooxidation. *J. Phys. Chem. C* **2013**, *117*, 13770–13775.
- (11) Roen, L. M.; Paik, C. H.; Jarvi, T. D. Electrocatalytic Corrosion of Carbon Support in PEMFC Cathodes. *Electrochem. Solid-State Lett.* **2004**, *7*, A19–A22.
- (12) Xu, J. F.; Fu, G. T.; Tang, Y. W.; Zhou, Y. M.; Chen, Y.; Lu, T. H. One-Pot Synthesis of Three-Dimensional Platinum Nanochain Networks as Stable and Active Electrocatalysts for Oxygen Reduction Reactions. *J. Mater. Chem.* **2012**, *22*, 13585–13590.
- (13) Tian, M.; Wu, G. S.; Chen, A. C. Unique Electrochemical Catalytic Behavior of Pt Nanoparticles Deposited on TiO₂ Nanotubes. *ACS Catal.* **2012**, *2*, 425–432.
- (14) Yu, T.; Zeng, J.; Lim, B.; Xia, Y. N.; Aqueous-Phase Synthesis of Pt/CeO₂ Hybrid Nanostructures and Their Catalytic Properties. *Adv. Mater.* **2010**, *22*, 5188–5192.
- (15) Lv, H. F.; Mu, S. C.; Cheng, N. C.; Pan, M. Nano-Silicon Carbide Supported Catalysts for PEM Fuel Cells with High Electrochemical Stability and Improved Performance by Addition of Carbon. *Appl. Catal., B* **2010**, *100*, 190–196.
- (16) Lv, H. F.; Peng, T.; Wu, P.; Pan, M.; Mu, S. C. Nano-Boron Carbide Supported Platinum Catalysts with much Enhanced Methanol Oxidation Activity and CO Tolerance. *J. Mater. Chem.* **2012**, *22*, 9155–9160.

- (17) Zhai, C. Y.; Zhu, M. S.; Bin, D.; Wang, H. W.; Du, Y. K.; Wang, C. Y.; Yang, P. Visible-Light-Assisted Electrocatalytic Oxidation of Methanol Using Reduced Graphene Oxide Modified Pt Nanoflowers-TiO₂ Nanotube Arrays. *ACS Appl. Mater. Interfaces* **2014**, *6*, 17753–17761.
- (18) He, C. L.; Jiang, Y. X.; Rao, L.; Wang, Q.; Zhang, B. W.; Li, Y. Y.; Sun, S. G. Synthesis of Ultrafine Size Platinum Nanoparticles on Defective Graphene with Enhanced Performance Towards Methanol Electro-Oxidation, *Fuel cells* **2013**, *5*, 873–880.
- (19) Zhao, L.; Wang, Z. B.; Li, J. L.; Zhang, J. J.; Sui, X. L.; Zhang, L. M. A Newly-Designed Sandwich-Structured Graphene–Pt–Graphene Catalyst with Improved Electrocatalytic Performance for Fuel Cells. *J. Mater. Chem. A* **2015**, *3*, 5313–5320.
- (20) Li, F. H.; Guo, Y. Q.; Liu, Y.; Yan, J.; Wang, W.; Gao, J. P. Excellent Electrocatalytic Performance of Pt Nanoparticles on Reduced Graphene Oxide Nanosheets Prepared by a Direct Redox Reaction Between Na₂PtCl₆ and Graphene Oxide. *Carbon* **2014**, *67*, 617–626.
- (21) Hummers Jr, W. S.; Offeman, R. E. Preparation of Graphitic Oxide. *J. Am. Chem. Soc.* **1958**, *80*, 1339.
- (22) Xu, Y. X.; Bai, H.; Lu, G. W.; Li, C.; Shi, G. Q. Flexible Graphene Films via the Filtration of Water-Soluble Noncovalent Functionalized Graphene Sheets. *J. Am. Chem. Soc.* **2008**, *130*, 5856–5857.
- (23) Xu, C.; Wang, X.; Zhu, J. W. Graphene-Metal Particle Nanocomposites. *J. Phys. Chem. C* **2008**, *112*, 19841–19845.

- (24) Xu, C.; Wang, X.; Zhu, J. W.; Yang, X. J.; Lu, L. D. Deposition of Co₃O₄ Nanoparticles onto Exfoliated Graphite Oxide Sheets. *J. Mater. Chem.* **2008**, *18*, 5625–5629.
- (25) Sun, Y. M.; Hu, X. L.; Luo, W.; Huang, Y. H. Self-Assembled Hierarchical MoO₂/Graphene Nanoarchitectures and Their Application as a High-Performance Anode Material for Lithium-Ion Batteries. *ACS Nano* **2011**, *5*, 7100–7107.
- (26) Tian, Z. F.; Liang, C. H.; Liu, J.; Zhang, H. M.; Zhang, L. D. Reactive and Photocatalytic Degradation of Various Water Contaminants by Laser Ablation-Derived SnO_x Nanoparticles in Liquid. *J. Mater. Chem.* **2011**, *21*, 18242–18247.
- (27) Tian, Z. F.; Liang, C. H.; Liu, J.; Zhang, H. M.; Zhang, L. D. Zinc Stannate Nanocubes and Nanourchins with High Photocatalytic Activity for Methyl Orange and 2,5-DCP Degradation. *J. Mater. Chem.* **2012**, *22*, 17210–17214.
- (28) Wu, S. L.; Wang, P. P.; Cai, Y. Y.; Liang, D. W.; Ye, Y. X.; Tian, Z. F.; Liu, J.; Liang, C. H. Reduced Graphene Oxide Anchored Magnetic ZnFe₂O₄ Nanoparticles with Enhanced Visible-light Photocatalytic Activity. *RSC Adv.* **2015**, *5*, 9069–9074.
- (29) Ye, Y. X.; Wang, P. P.; Dai, E. M.; Liu, J.; Tian, Z. F.; Liang, C. H.; Shao, G. S. A Novel Reduction Approach to Fabricate Quantum-sized SnO₂-Conjugated Reduced Graphene Oxide Nanocomposites as Non-Enzymatic Glucose Sensors. *Phys. Chem. Chem. Phys.* **2014**, *16*, 8801–8807.
- (30) Anandan, S.; Manivel, A.; Ashokkumar, M. One-Step Sonochemical Synthesis of Reduced Graphene Oxide/Pt/Sn Hybrid Materials and Their Electrochemical Properties. *Fuel Cells* **2012**, *6*, 956–962.

- (31) Ding, L. X.; Wang, A. L.; Li, G. R.; Liu, Z. Q.; Zhao, W. X.; Su, C. Y.; Tong, Y. X. Porous Pt-Ni-P Composite Nanotube Arrays: Highly Electroactive and Durable Catalysts for Methanol Electrooxidation. *J. Am. Chem. Soc.* **2012**, *134*, 5730–5733.
- (32) Hao, Y. F.; Yang, Y. Y.; Hong, L. J.; Yuan, J. H.; Niu, L.; Gui, Y. H. Facile Preparation of Ultralong Dendritic PtIrTe Nanotubes and Their High Electrocatalytic Activity on Methanol Oxidation. *ACS Appl. Mater. Interfaces* **2014**, *6*, 21986–21994.

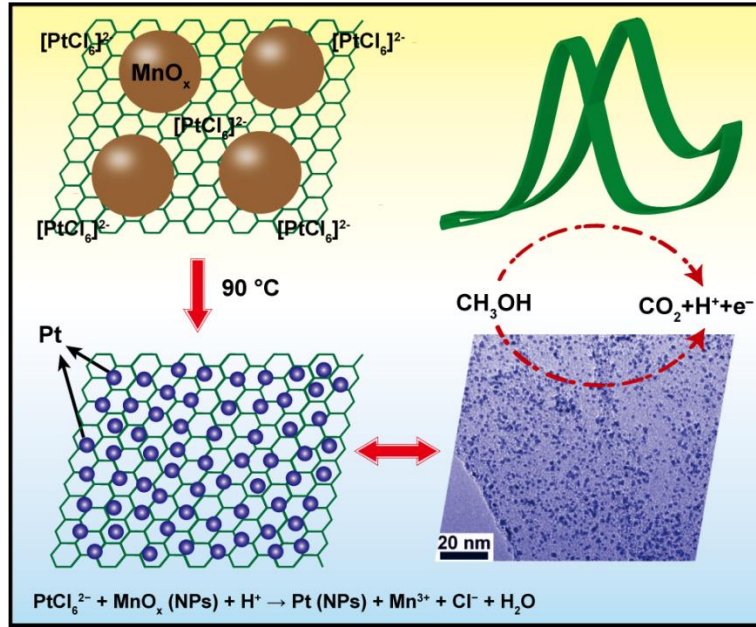


Figure for Graphical abstract